Environmental Pollution 306 (2022) 119424

Contents lists available at ScienceDirect

Environmental Pollution

journal homepage: www.elsevier.com/locate/envpol

Source analysis of the tropospheric NO_2 based on MAX-DOAS measurements in northeastern China☆

Feng Liu [a], Chengzhi Xing [d], Pinjie Su [a], Yifu Luo [a], Ting Zhao [a], Jiexiao Xue [a], Guohui Zhang [a], Sida Qin [b], Youtao Song [a], Naishun Bu [a,c,*]

[a] School of Environmental Science, Liaoning University, Shenyang, 110036, China
[b] Liaoning Science and Technology Center for Ecological and Environmental Protection, Shenyang, 110161, China
[c] Key Laboratory of Wetland Ecology and Environment Research in Cold Regions of Heilongjiang Province, Harbin University, 150086, China
[d] Key Lab of Environmental Optics & Technology, Anhui Institute of Optics and Fine Mechanics, Hefei Institutes of Physical Science, Chinese Academy of Sciences, Hefei, 230031, China

ARTICLE INFO

Keywords:
MAX-DOAS
NO_2
GAM
Source analysis

ABSTRACT

Ground-based Multi-Axis Differential Optical Absorption Spectroscopy (Max-DOAS) measurements of nitrogen dioxide (NO_2) were continuously obtained from January to November 2019 in northeastern China (NEC). Seasonal variations in the mean NO_2 vertical column densities (VCDs) were apparent, with a maximum of 2.9×10^{16} molecules cm^{-2} in the winter due to enhanced NO_2 emissions from coal-fired winter heating, a longer photochemical lifetime and atmospheric transport. Daily maximum and minimum NO_2 VCDs were observed, independent of the season, at around 11:00 and 13:00 local time, respectively, and the most obvious increases and decreases occurred in the winter and autumn, respectively. The mean diurnal NO_2 VCDs at 11:00 increased to at 08:00 by 1.6, 5.8, and 6.7×10^{15} molecules cm^{-2} in the summer, autumn and winter, respectively, due to increased NO_2 emissions, and then decreased by 2.8, 4.2, and 5.1×10^{15} molecules cm^{-2} at 13:00 in the spring, summer, and autumn, respectively. This was due to strong solar radiation and increased planetary boundary layer height. There was no obvious weekend effect, and the NO_2 VCDs only decreased by about 10% on the weekends. We evaluated the contributions of emissions and transport in the different seasons to the NO_2 VCDs using a generalized additive model, where the contributions of local emissions to the total in the spring, summer, autumn, and winter were 89 ± 12%, 92 ± 11%, 86 ± 12%, and 72 ± 16%, respectively. The contribution of regional transport reached 26% in the winter, and this high contribution value was mainly correlated with the northeast wind, which was due to the transport channel of air pollutants along the Changbai Mountains in NEC. The NO_2/SO_2 ratio was used to identify NO_2 from industrial sources and vehicle exhaust. The contribution of industrial NO_2 VCD sources was >66.3 ± 16% in Shenyang due to the large amount of coal combustion from heavy industrial activity, which emitted large amounts of NO_2. Our results suggest that air quality management in Shenyang should consider reductions in local NO_2 emissions from industrial sources along with regional cooperative control.

1. Introduction

Nitrogen dioxide (NO_2) plays a vital role in atmospheric chemistry and participates in the formation of nitric acid rain, secondary aerosols and tropospheric ozone (Crutzen, 1970; Lelieveld et al., 2002; Stavrakou et al., 2013; Valin et al., 2013). NO_2 emissions in China have been high at 1.5 million t/a during the past 10 years (Rollins et al., 2012; Yang et al., 2019), and the spatiotemporal distribution of tropospheric NO_2 has shown to be heterogeneous due to its relatively short lifetime and different sources (Wang et al., 2020). Thus it is important to investigate the spatial and temporal patterns of NO_2 concentrations and NO_2 sources to implement effective air pollution control and air quality management measures.

Most NO_2 emissions originate from ambient combustion processes, such as fossil fuel combustion, biomass burning and lightning (Wu et al., 2018; Adame et al., 2020). Among these processes, major sources of NO_2

☆ This paper has been recommended for acceptance by Admir Créso Targino.

* Corresponding author. School of Environmental Science, Liaoning University, Shenyang, 110036, China.
E-mail address: bunaishun@lnu.edu.cn (N. Bu).

https://doi.org/10.1016/j.envpol.2022.119424
Received 20 April 2021; Received in revised form 3 May 2022; Accepted 4 May 2022
Available online 7 May 2022
0269-7491/© 2022 Elsevier Ltd. All rights reserved.

include vehicle exhaust and industrial activity, both of which result in high levels of fossil fuel combustion (Shen et al., 2021). Due to differences in energy demands and industrial structures, the primary sources of NO_2 will vary in different regions (Hong et al., 2018; Song et al., 2019). Regional transport from other regions is another key source of NO_2 (Hong et al., 2019). For example, Feng et al. (2019) found that regional transport accounted for 32% of NO_2 concentration in Hangzhou. Jeong et al. (2017) reported that the contribution of long-range transport to the mean NO_2 concentration in Seoul was 3.4 ppb in 2014, which accounted for 9% of the mean concentration compared to 2001. These studies concluded that regional transport and local emissions contributed to NO_2 concentrations. Therefore, it is important to quantify the contributions of the different sources of NO_2 to support NO_2 control measures.

Most previous studies have investigated NO_2 sources using data obtained from satellite observations and *in situ* measurements (Lamsal et al., 2014; Guo et al., 2016; Tian et al., 2020; Wyche et al., 2021). However, these techniques have some notable disadvantages. For example, Hong et al. (2019) showed that the regional transport of air pollutants occurred at both the ground level and higher altitudes. However, *in situ* measurements will be limited to the vicinity of the ground (Song et al., 2015), and satellite observations do not provide sufficient sensitivity in the lower troposphere and do not provide vertical information (Tao et al., 2012; Zhang et al., 2017, 2019, 2020). By contrast, multi-axis differential optical absorption spectroscopy (MAX-DOAS) is a ground-based passive remote sensing technique (Hönninger et al., 2004; Letu et al., 2021; Platt and Stutz, 2008; Ou et al., 2021; Wittrock et al., 2004; Xing et al., 2019), which has the advantage of monitoring the vertical column density and vertical profile of NO_2 compared to the above techniques (Hendrick et al., 2014; Vlemmix et al., 2011; Xing et al., 2017, 2020). Because of its simple experimental setup, this process offers relatively high sensitivity and continuity; thus, MAX-DOAS has been widely used to measure atmospheric NO_2 concentrations (Li et al., 2012; Hendrick et al., 2014; Takashima et al., 2015; Wang et al., 2017; Chan et al., 2018; Cheng et al., 2019; Chan et al., 2020). MAX-DOAS can also provide information regarding the vertical distribution of NO_2 to support the study of regional NO_2 transport. Yang et al. (2019) reported that local emissions, rather than regional transport, were the largest contributor of NO_2 during the heating season in Hefei based on MAX-DOAS observations. Tan et al. (2020) used both MAX-DOAS data and weather research and forecasting model-simulated wind field information to quantify NO_2 transportation flux from northern Jiangsu to the Anhui Province during the haze pollution period. Therefore, MAX-DOAS measurements may be suitable for obtaining the spatiotemporal distribution of NO_2 and analyzing NO_2 sources.

Northeastern China (NEC) is located at high latitudes. Due to the low perennial temperature in this region, coal combustion is often used for heating in winter (Li et al., 2020a, 2020b), which combined with the blocking effect of the southeast mountains readily causes air pollution events. Zhao et al. (2020) found a pollution transport belt across northern China and into NEC along the coast. Shenyang is the economic, industrial and transportation center of NEC (Yang et al., 2020), and it is dominated by the machinery industry, which is mainly located in the Tiexi District. Previous studies have shown that NO_2 pollution in Shenyang is associated with local emissions and regional transport from surrounding areas (e.g., the Beijing-Tianjin-Hebei, Shandong and Inner Mongolia Autonomous regions) (Miao et al., 2018; Ma et al., 2019). However, these studies usually have typically *in situ* measurements that were limited to the ground surface and could easily underestimate the transport effect.

In this study, tropospheric NO_2 sources in Shenyang were analyzed using MAX-DOAS measurements. Section 2 presents a detailed introduction to the measurement instrument, data retrieval, generalized additive model (GAM) simulation, application of the NO_2/SO_2 ratios, and the ancillary data. Analysis of the temporal characteristics of the NO_2 vertical column densities (VCDs), as well as a comparison with the ozone monitoring instrument (OMI) satellite observations are presented in sections 3.1 and 3.2, respectively. The contributions of local emissions and regional transport toward the NO_2 VCDs, as well as the relative contributions of the industrial sources and vehicle emissions to the NO_2 emissions are presented in sections 4.1 and 4.2 The conclusions are presented in section 5.

2. Measurements and methodology

2.1. MAX-DOAS measurements

2.1.1. Experimental setup

The MAX-DOAS system for monitoring NO_2 VCDs was operated from January 2019 to November 2019 on the roof of the Huixing building at Liaoning University (41°55′N, 123°23′E) (Fig. 1). The MAX-DOAS instrument operated automatically, and it consisted of three major parts: a telescope unit, two spectrometers with a stabilized temperature of 20 °C, and a computer, which served as the control terminal and data collection unit. The scattered sunlight collected by the telescope, and its change in viewing elevation angle were controlled by a stepping motor. The ultraviolet (UV) and visible wavelength ranges of the two spectrometers (Acton Spectrapro 300i Czerny-Turner Optical Spectrometer) were 300–460 nm and 400–560 nm, respectively. Only the UV wavelength range was used to retrieve the NO_2 and SO_2 differential slant column densities (DSCDs) in this study. The spectral resolution of the spectrometers, in terms of the full width at half maximum was 0.6 nm. Two optical spectrometers were equipped with 2048-pixel charge coupled device detector cameras (model DU 440-BU).

The full measurement scanning sequence of the telescope included 11 elevation angles, of 1, 2, 3, 4, 5, 6, 8, 10, 15, 30, and 90°. In this study, only the 30° and 90° elevations were used to calculate the NO_2 geometric VCDs; however, the full elevation scan will be used to retrieve the NO_2 profiles in future work. The exposure time of each elevation angle measurement was fixed at 60 s, while the azimuth angle of the telescope was fixed at 56° (north = 0°). The field of view was estimated to be less than 0.3°. The dark current and offset were measured every night.

2.1.2. Spectral analysis

In this study, the QDOAS software developed by the Royal Belgian Institute for Space Aeronomy (BIRA-IASB) (http://uv-vis.aeronomie.be/software/QDOAS/) was used for analyzing the measurement spectra. The details of the NO_2 and SO_2 retrieval settings are presented in Table 1. The spectrum measured with a scan zenith of 90° was selected as the reference spectrum in each scan set to remove the effects of absorption in the stratosphere. Prior to spectral analysis, the offset spectra and dark current were subtracted from the measured spectra, and the DSCDs were the direct result of the DOAS fit which was applied to a wavelength range from 338 to 370 nm to retrieve the DSCDs of the NO_2 in this study (Table 1). Fig. 2 shows a typical example of QDOAS retrieval from the MAX-DOAS spectrum obtained at 8° on January 29th, 2019 at a solar zenith angle (SZA) of 54.35°. The root mean square (RMS), NO_2 DSCD and NO_2 DSCD errors were 3.06×10^{-4}, 1.57×10^{17}, and 7.74×10^{14} molecules cm^{-2}, respectively. The data for NO_2 DSCDs were filtered when the RMS value of the residuals was greater than 2.5×10^{-3} and the SZA was greater than 80°.

2.1.3. Determination of tropospheric NO_2 VCD

Because the DSCD was dependent on the position and viewing direction of the MAX-DOAS, the NO_2 slant column density (SCD) was converted to the VCD using the air mass factor (AMF). The tropospheric DSCD ($DSCD_{Trop(\alpha)}$) of a trace gas can be obtained by subtracting the DSCD of the observation spectrum of the zenith direction ($\alpha \neq 90°$) and the azimuth direction ($\alpha = 90°$) in the same observation sequence of MAX-DOAS. The equation is given by:

Fig. 1. Location of the measurement sites and topography of the surrounding region.

Table 1
The parameter settings used in the MAX-DOAS analysis.

Parameter	Data Source	Fitting interval	
		NO_2	SO_2
Wavelength range		338–370 nm	305–317.5 nm
NO_2	298 K, I_0[a] correction (SCD of 10^{17} molecules/cm^2); Vandaele et al. (1998)	✓	✓
NO_2	220 K, I_0[a] correction (SCD of 10^{17} molecules/cm^2), pre-orthogonalized; Vandaele et al. (1998)	✓	×
O_3	223 K, I_0 correction (SCD of 10^{20} molecules/cm^2); Serdyuchenko et al. (2014)	✓	✓
O_3	243 K, I_0 correction (SCD of 10^{20} molecules/cm^2), pre-orthogonalized; Serdyuchenko et al. (2014)	✓	✓
O_4	293 K; Thalman and Volkamer (2013)	✓	×
BrO	223 K; Fleischmann et al. (2004)	✓	✓
SO_2	293 K; Bogumil et al. (2003)	×	✓
Ring	Calculated with QDOAS	✓	×
Polynomial degree		Order 5	Order 5
Intensity offset		Constant	Constant

[a] Solar I_0 correction; (Aliwell et al., 2002).

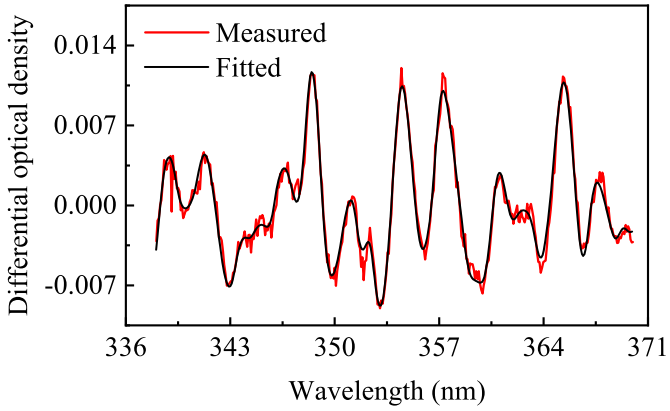

Fig. 2. Example of the DOAS retrieval of the NO_2 DSCDs. The black lines represents the absorption signal and the red line represents the sum of the absorption signal and the fit residual. (For interpretation of the references to colour in this figure legend, the reader is referred to the Web version of this article.)

$$VCD_{Trop} = \frac{DSCD_{Trop(\alpha)}}{DAMF_{Trop(\alpha)}} = \frac{SCD_{Trop(\alpha)} - SCD_{Trop(90^\circ)}}{AMF_{Trop(\alpha)} - AMF_{Trop(90^\circ)}}, \quad (1)$$

where VCD_{Trop} is the tropospheric VCD of the trace gas, and $DAMF_{Trop(\alpha)}$ is the differential tropospheric atmospheric AMF between $\alpha \neq 90^\circ$ and $\alpha = 90^\circ$.

The AMF could be calculated quickly using the geometric approximation method, which has been a widely used method validated using the radiative transfer model (RTM) calculation method. The time series of the NO_2 VCDs obtained from the geometric AMF ($AMF = 1/\sin_{(\alpha)}$) and RTM AMF were in good agreement, and the difference between them

was about 20%–30%. Thus, the 30° elevation angle measurements of the campaigns were the most appropriate for the geometric approach. The possible biases arising from the geometric approximation AMF calculation will typically be smaller than those calculated through that RTM model for an elevation angle of 30°, with a bias of <20%. Thus, the error in the AMF calculations using the geometric approximation would mainly depend on the vertical aerosol distributions. The uncertainty of the AMF calculations caused by the aerosol profiles at different wavelengths was determined by a sensitivity study, and we found that the average effect of different aerosol profiles on the AMF calculation results for NO_2 (SZAs were less than 75°) was 11% (Fig. S1), according to the equation:

$$VCD_{err} = \frac{DSCD_{err}}{DAMF_{err}}, \tag{2}$$

where the VCD errors (VCD_{err}) originated from the DSCD errors ($DSCD_{err}$) and the DAMF errors ($DAMF_{err}$). The DSCD errors were caused by DOAS analysis progress, and in this study, the $DAMF_{err}$ were defined as the difference between the geometrical AMF and the RTM AMF. The DSCD errors in this study were calculated through DOAS fittings (Fig. S2), where the DAMF errors were set to 20%, 25%, and 30% (i.e., 20%–30%) in the summer, spring (autumn), and winter, respectively. The large error in winter was mainly due to the heavy aerosol load.

The DSCDs of NO_2 and SO_2 were measured at an elevation angle of 30° to calculate their VCDs. Because 1/sin (30°) = 2, the DSCDs measured at an elevation angle of 30° were equal to the VCDs. Therefore, an elevation angle of 30° was used in the VCD_{Trop} and error calculations due to the geometrical approximation in this study, where VCD_{Trop} was expressed by:

$$VCD_{Trop} = \frac{DSCD_{Trop(\alpha)}}{\frac{1}{sin_{(\alpha)}} - 1}. \tag{3}$$

2.2. GAM simulation

The GAM allowed for the addition of non-linear variance functions by generalizing the linear regressions. It could also be used to fit non-linear relationships automatically without attempting different transformations manually.

A GAM requires less data; thus it could be applied to different types of distributions (e.g., normal distributions), and used to measure the effects of explanatory variables on the response variables using different functions (e.g., inverse, logarithmic, and other link functions). The GAM for the daily NO_2 concentration series used the logarithmic function as the link function, according to the following equation:

$$log(y) \sim \beta + \sum_{i}^{n} S(X_i) + \varepsilon, \tag{4}$$

where y is the response variable, β is the constant mean of y, X_i is an explanatory variable that drives or intercepts y, $S(X_i)$ is the ith smoothing function of the covariate for the ith sample, and ε is the ith residual, assuming that $\varepsilon \sim N(0, \sigma^2)$.

In this study, the GAM was implemented to assess the contributions of emissions and transportation toward the NO_2 concentrations. This study considered the average daily NO_2 VCDs obtained from the MAX-DOAS measurements as the response variable, while the daily average of relevant influencing factors was the explanatory variable. The GAM model revealed the percentages of contributions from the local emissions and transport from the other regions toward the NO_2 VCDs and the total NO_2 concentration.

2.3. NO_2/SO_2 ratios

To identify the main sources of NO_2 emissions, the contributions of different sources toward the emitted NO_2 were estimated using the NO_2/SO_2 ratios. The NO_2 and SO_2 VCDs were obtained from the MAX-DOAS measurements. The ambient NO_2/SO_2 ratio was approximately equal to the ratio of NO_2/SO_2 emissions because NO_2 and SO_2 had approximately the same lifetime. The NO_2 VCDs and SO_2 VCDs exhibited a good correlation (R = 0.82) (Fig. S3), indicating that ambient NO_2 and SO_2 had generally similar emission sources. Moreover, because vehicles mainly emit NO_2 instead of SO_2, while heavy industry emits both NO_2 and SO_2 due to the use of fossil fuels that contain sulfides, a low NO_2/SO_2 ratio indicated higher industrial sources. By contrast, high NO_2/SO_2 ratio implied that vehicle emissions make a large contribution to the NO_2 VCDs.

In this study, we assumed that ambient NO_2 was mainly emitted from industrial and vehicle sources, and natural and other anthropogenic sources of NO_2 were not considered. Linear regression of the NO_2 and SO_2 VCDs was performed to calculate the slope (NO_2/SO_2) and intercept. Thus, a linear orthogonal regression was used, where the orthogonal difference was used for slope estimation, rather than the x- or y-errors. The slope and intercept were used to estimate the contributions of the industrial ($P_{industrial\ sources}$) and vehicle ($P_{vehicle\ sources}$) sources to the emitted NO_2. These contributions can be calculated using the following equations:

$$P_{industrial\ sources} = \frac{NO_2(industrial\ sources)}{NO_2} \times 100\%, \tag{5}$$

$$= \frac{SO_2 \times slope + intercept}{NO_2} \times 100\%, \tag{6}$$

$$P_{vehicle\ sources} = \frac{NO_2(vehicle\ exhaust)}{NO_2} \times 100\%, \tag{7}$$

$$= \frac{NO_2 - (SO_2 \times slope + intercept)}{NO_2} \times 100\%, \tag{8}$$

where SO_2 and NO_2 denote the SO_2 and NO_2 VCDs, respectively, and the linear regression slope and intercept were 1.08 and 0.48, respectively (Fig. S3).

The impact of error estimation on the regression results was calculated using Equations (6) and (8). The errors of the regression results were 16%, 13%, 15%, and 19% in spring, summer, autumn and winter, respectively.

2.4. Ancillary data

The meteorological variables (i.e., wind speed, wind direction, relative humidity, air temperature and precipitation) used in the GAM simulation were measured at Taoxian Airport in Shenyang (http://www.wunderground.com, last access: 18 April 2021), which was approximately 22.6 km away from the monitoring site used in this study. The temporal resolution of these meteorological data was 30 min, and this study focused on the effects of wind speed and wind direction on the NO_2 concentration in the GAM. The planetary boundary layer height values (PBLH) (CALIPSO Lidar Level 2, Validated Stage 1 V4-02) were obtained from the National Aeronautics and Space Administration (NASA) (https://disc.gsfc.nasa.gov/, last access: 18 July 2021). The particulate matter (PM) concentrations were obtained from the Lingdongjie monitoring station at the China National Environmental Monitoring Centre (CNEMC) network (41.84°N, 123.42°E) (http://www.cnemc.cn/, last access: 2 October 2021), which was about 1.5 km from the monitoring site.

This study compared the MAX-DOAS measurements and OMI (TROPOMI) NO_2 (SO_2) VCDs. Retrieval of the NO_2 SCDs from the OMI was accomplished using the DOAS method and by converting the SCDs to VCDs using the AMF. The OMI level-3 gridded NO_2 product (OMNO2d) was obtained from the NASA Goddard Earth Sciences Data and Information Services Center (GES-DISC) (https://disc.gsfc.nasa.gov/, last access: 18 April 2021), and the Level 2 offline SO_2 dataset

(S5P_OFFL_L2_SO2_) version 1.01.07 was obtained from the European Space Agency (ESA)-Copernicus Sentinel-5P Pre-Operation Data-Hub (https://s5phub.copernicus.eu/, last access: 5 October 2021). The OMNO2d consisted of a daily data product with a 0.25° × 0.25° latitude-longitude grid, with a spatial resolution o about 13 × 24 km^2. The gridded OMI VCDs within 15 km of the measurement site (i.e., the approximate average OMI pixel size) were averaged to monthly values and compared with the MAX-DOAS time series. The overpass time of the OMI satellite in the Shenyang region was around 13:30 local time. The effective cloud fractions (CFs) and cloud top heights (CTHs) were obtained from the Tropospheric Emission Monitoring Internet Service (TEMIS) for OMI retrieval, where CFs greater than 30% were excluded from the comparison.

3. Results

3.1. Overview of the tropospheric NO_2

The seasonal variations in the tropospheric NO_2 VCDs exhibited a maximum value of 2.9 × 10^{16} molecules cm^{-2} in January and a minimum value of 1.4 × 10^{16} molecules cm^{-2} in May (Fig. S4). In addition, the monthly averaged tropospheric NO_2 VCDs were compared at 15° and 30° (Fig. S5). In this study, the spring, summer, autumn and winter seasons were defined as March to May, June to August, September to November, and January to February, respectively. In December, the instrument failed, and it was removed and sent back to the manufacturer for maintenance. January and February could be used to characterize winter. The averaged seasonal NO_2 VCDs were 1.8 × 10^{16}, 2.1 × 10^{16}, 2.0 × 10^{16}, and 2.9 × 10^{16} molecules cm^{-2} in the spring, summer, autumn and winter, respectively (Fig. 3). Shenyang typically has a long and harsh winter, and January is the coldest month of the year with an average temperature of −16 °C. The heating season starts earlier and lasts longer, i.e., for about 6 months (November–April), in Shenyang compared to other cities in China. This increased consumption of fossil fuels and biofuels during the heating season will partly contribute to the maximum NO_2 VCDs in winter, especially as people rely more on motor vehicles than walking in winter, resulting in increased traffic emissions. However, the oxidation of the hydroxyl radical (OH) has shown to be a key pathway for the NO_2 sink pathway in the troposphere, and the OH concentrations reached a minimum value in winter, causing the lifetime of NO_2 to be longer in winter than that in other seasons. In addition to the emissions and photochemical processes that affect the seasonal pattern of the NO_2 VCDs, meteorological conditions have also been shown to play an important role in the high NO_2 concentrations in winter. Shenyang is surrounded by heavily polluted areas, and the transport of pollutants under the influence of southern winds may decrease the air quality in Shenyang in winter. Therefore, regional NO_2 transport from nearby polluted areas may increase the NO_2 concentrations in winter.

The diurnal variations in the NO_2 VCDs at elevation angles of 15° and 30° in spring, summer, autumn, and winter are shown in Fig. S6 and 4, respectively. We found that there was an initial increase in the NO_2 VCDs at all times; however, this was extended in winter. The diurnal variations in NO_2 VCDs increased by 1.6 × 10^{15}, 5.8 × 10^{15}, and 6.7 × 10^{15} molecules cm^{-2} from 08:00 to 11:00 in summer, autumn, and winter at an elevation angle of 30°, respectively, while the NO_2 VCDs decreased between 11:00 and 14:00 in the summer (from 1.8 to 1.6 × 10^{16} molecules cm^{-2}), spring (from 2.2 to 1.8 × 10^{16} molecules cm^{-2}), and autumn (from 2.4 to 1.9 × 10^{16} molecules cm^{-2}) at an elevation angle of 30°. This reduction was associated with high photochemical NO_2 loss around noon, and the elevated PBLH increased the NO_2 mixing area (Fig. S7). Interestingly, the NO_2 VCDs lagged by about 2 h in the winter compared to the other three seasons (Fig. 3). One reason for this was that the peak travel time was delayed during the winter. Additional reasons include the relatively weaker removal capacity and weak diffusion conditions of NO_2 in winter compared to the other seasons.

The weekend effect was defined as a reduction in industrial activity and traffic volume, resulting in lower concentrations of pollutant emissions during the weekend. The weekend effect has shown to be significant in most western countries; however, this effect was not found in most Chinese cities (Beirle et al., 2003). This was due to the continuous industrial activity throughout the week and the fact that there are no formal weekly breaks in China (Javed et al., 2019). In this study, the measured NO_2 VCDs decreased by less than 10% on weekends compared to weekdays (Fig. 4). By contrast, a pronounced reduction of 20%–35% occurred in the NO_2 VCDs in the Baoshan district of Shanghai. The Baoshan district is a semi-industrial area with light industrial activity, with reduced the NO_2 emissions over the weekend. Shenyang is a heavy industrial city with a large workload, power plants, and heavy industrial work throughout the week, which did not show an obvious reduction in NO_2 emissions during the weekend. The NO_2 concentrations on weekends at 9:00 were higher than that on weekdays (Fig. 4). The increase in PM concentration was related to the decrease in visibility caused by increased human activity, resulting in a decrease in the NO_2 photolysis rate. The diurnal variations in the PM concentration during the weekly

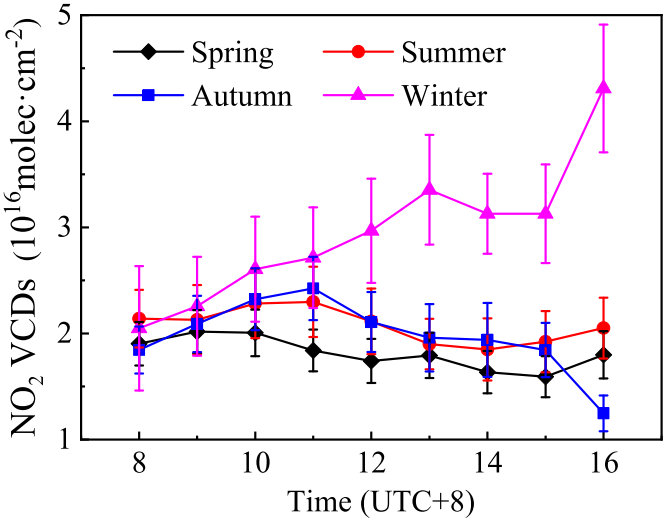

Fig. 3. Seasonally averaged diurnal variations in the tropospheric NO_2 VCDs from the MAX-DOAS measurements. The error bars represent the ratios of the DSCD and DAMF errors.

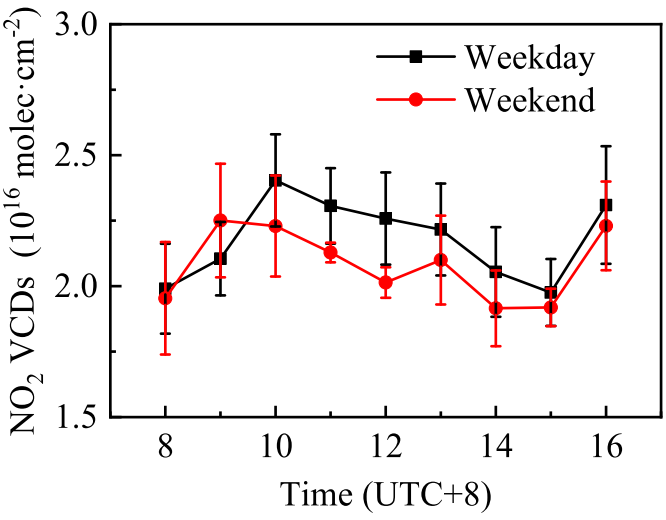

Fig. 4. Weekly cycle of the diurnal variations in the tropospheric NO_2 VCDs retrieved by MAX-DOAS. The error bars represent the ratios of the DSCD and DAMF errors.

cycle verified the conjecture in Fig. S8.

3.2. Comparison with OMI NO_2

The MAX-DOAS measurements and the OMI (TROPOMI) NO_2 (SO_2) VCDs were compared. For better comparison, the MAX-DOAS results within ±1 h of the OMI (TROPOMI) satellite overpass time were used. The MAX-DOAS and OMI measurements of the NO_2 VCDs showed a good correlation, with a Pearson correlation coefficient of R = 0.73 (Fig. 5b), while the SO_2 VCDs showed a poor correlation at R = 0.39 (Fig. 9Sb). However, the NO_2 and SO_2 VCDs of the satellite observations were systematically lower than the MAX-DOAS measurements for all months (Figs. 5a and 9Sa). These discrepancies were related to the different spatial coverages of the two observation methods and the large-area averaging effect, including the clean OMI observation regions, which has possibly led to an underestimation of pollution hotspots around the world by about 20%–50%. In addition, the cloud cover, aerosol shielding effect, and low sensitivity to near-surface NO_2 and SO_2 of the OMI (TROPOMI) observations also contributed to these discrepancies.

4. Discussion

4.1. Evaluating the contributions of emissions and transport toward the NO_2 concentration

Local emissions and regional transport can affect air pollution (Zhao et al., 2020). Thus, to assess the contributions of local emissions and transportation toward the NO_2 concentrations, a statistical fitting approach was implemented based on GAM. We found that local emissions contributed 89 ± 12%, 92 ± 11%, 86 ± 12%, and 72 ± 16% to the measured NO_2 concentrations in the spring, summer, autumn and winter, respectively, while the contributions of transport were only 9%, 6%, 11%, and 26% during the four seasons, respectively (Fig. 6). The higher contribution of local emissions suggested that NO_2 could be mainly attributed to emissions from local sources in all seasons. Shenyang was influenced by southwest wind (Fig. 7) and short-range transport from the Tiexi District (an old industrial base) may have partly contributed to the changes in the NO_2 concentrations at the observation site (Fig. S10). The highest contribution of local emissions was observed in the summer, reaching 1.7–2.1 × 10^{16} molecules cm^{-2}. A lower wind speed (mostly <4 m s^{-1}) (Fig. 7) and weak diffusion conditions led to local NO_2 accumulation, and the shorter photochemical lifetime of NO_2 in the atmosphere during summer limited long-range NO_2 transport (Li et al., 2016).

Although domestic coal-fired heating increased local emissions during winter, regional transport still made a large contribution to the NO_2 concentration during this season at 26%, which was higher

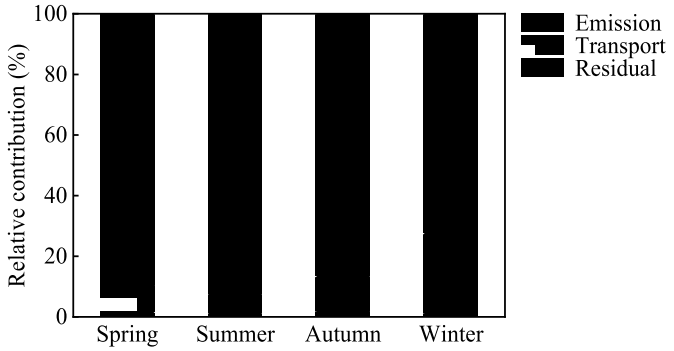

Fig. 6. Contributions of local emissions and transport toward the NO_2 concentrations.

compared to its contributions in other seasons (Fig. 6). This large contribution showed that regional transport was an essential source of NO_2. Shenyang frequently experiences northeast winds with high wind speeds (3–6 m s^{-1}) in the winter (Fig. 7). The northeast area also hosted more industrial activities and had more vehicles in operation. This led to significant NO_2 emissions, which were transported to the observation site by under the prevailing northeast wind. Topography has been shown to affect the wind fields that drive the regional transport of pollutants (Quan et al., 2020), and NEC is surrounded by the Xiaoxinganling Mountains, the Greater Khingan Mountains and the Changbai Mountains to the north, west, and east, respectively. Thus, a transport channel of air pollutants existed from the northeast to the southwest along the Changbai Mountains of NEC. Polluted air originating from the northeast was transported to areas at low altitudes in the southwest by the northeast wind in winter (Fig. 7). Liaoning Province, located southwest of the Jilin and Heilongjiang provinces, is typically cold in winter with a greater need for burning coal for heating. Therefore, the air masses from the northeast passed through these regions, and more NO_2 was transferred during air transport from the polluted upwind areas to Liaoning Province. The results of this study suggest that local emission reductions and regional cooperative control should be considered when managing air quality in Shenyang.

4.2. Possible contributions to NO_2 emissions

Industrial sources and vehicle emissions have shown to be the two major contributors to anthropogenic NO_2 emissions in Shenyang (Gao et al., 2020). Thus, it is important to understand the individual contributions of industrial NO_2 emissions and vehicle exhaust toward NO_2 emissions in order to design appropriate NO_2 emission control strategies. The results of this study showed that the contributions of industrial

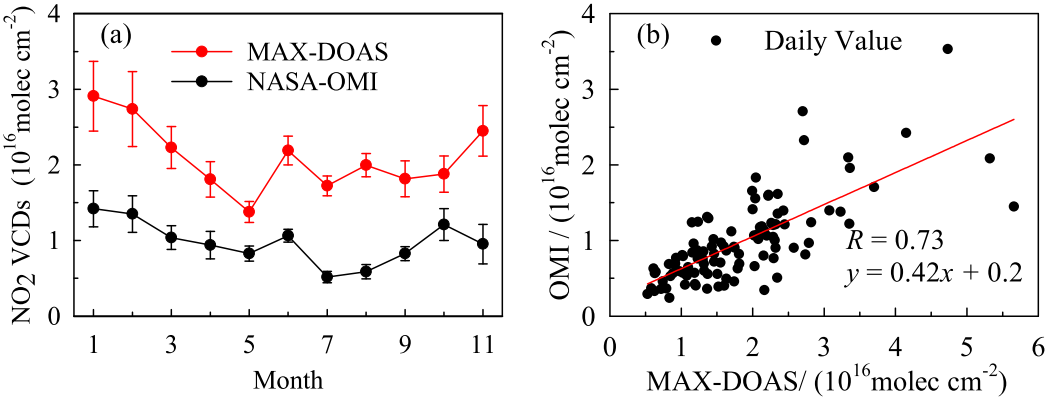

Fig. 5. Comparison of the tropospheric NO_2 VCDs obtained by the MAX-DOAS measurements and by the OMI satellite observations. (a) Time series of tropospheric NO_2 VCDs. (b) The correlation between the tropospheric NO_2 VCDs measured using MAX-DOAS and the NASA-OMI satellite data.

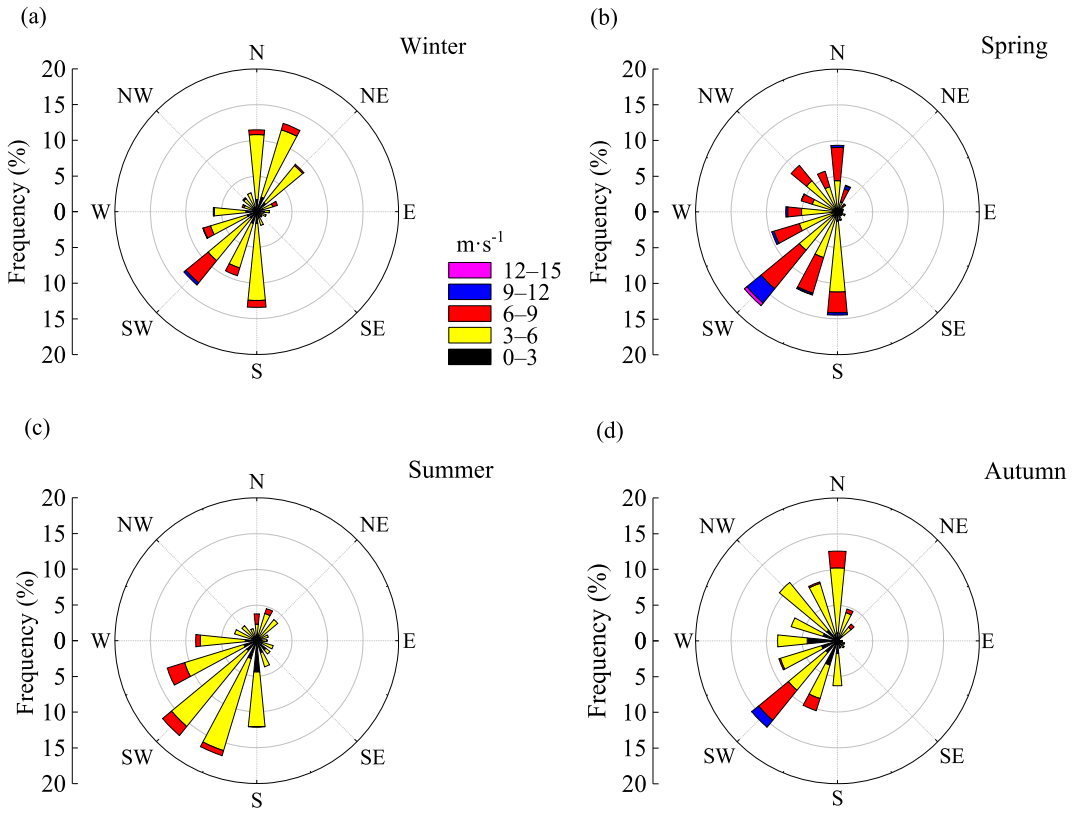

Fig. 7. Wind rose diagrams based on all of hourly averaged observations of the weather station for (a) winter, (b)spring, (c) summer and (d) autumn.

sources toward the NO_2 concentrations were 75.3%, 66.3%, 76.6%, and 83.5% in the spring, summer, autumn and winter, respectively (Fig. 8). Shenyang was a heavily industrialized city in China that with 1107 industries in 2019, and coal consumption in Shenyang was 2.8×10^7 t in 2019, while the coal utilization by the industry was 8.5×10^6 t (Statistical Yearbook of Shenyang, 2020). This accounted for about one-third of the total coal consumption in Shenyang. Excessive fossil fuel combustion by industrial activity enhanced NO_2 emissions. The government has taken aggressive measures in recent years to control vehicle exhaust pollution by reducing NO_2 emissions from mobile sources, such as by implementing strict vehicle emission standards and promoting energy transition from fossil fuels to cleaner fuels. The contribution of industrial sources toward NO_2 concentrations in winter was higher than in other seasons (Fig. 8). This phenomenon may be associated with increased coal combustion for heating, which released significant amounts of NO_2 during the winter. Moreover, in Shenyang, about 90% of winter heating depends on the combustion of coal in. Therefore, it is necessary to control NO_2 emissions from coal combustion to improve the air quality during winter (Li et al., 2019). These results showed that industrial emissions played a dominant role in local emissions in Shenyang, and placing an emphasis on reducing NO_2 emissions from industry is important in to mitigate air pollution.

The coordinated control of $PM_{2.5}$ and O_3 and coordinated regional governance have been the primary tasks of the 14th Five-Year Plan in China. NO_2 is a key precursor of $PM_{2.5}$ and O_3, and mainly derived from emissions. Therefore, the control and reduction of NO_2 emissions will be the key to achieving the coordinated control of $PM_{2.5}$ and O_3. These results indicated that controlling local NO_2 emissions will be necessary to improve the air quality in Shenyang. In addition, regional NO_2 transport from the northeastern regions may have an impact on the air quality in Shenyang, suggesting that NO_2 pollution cannot be eliminated solely by reducing local emissions. To continuously improve air quality, it is important to strengthen the coordinated control of regional collaborative governance. These findings may be useful for designing collaborative strategies for air pollution control on the regional scale in NEC.

5. Conclusions

MAX-DOAS observations were conducted in Shenyang to measure the tropospheric NO_2 from January to November 2019. The tropospheric NO_2 VCDs showed maximum values in January due to increased emissions from heating. The NO_2 VCDs increased from 08:00 to 11:00 and then decreased slightly at noon. The OMI and MAX-DOAS measurements of the NO_2 VCDs showed a good correlation ($R = 0.73$). The NO_2 mainly originated from local emissions in Shenyang in all seasons, and the largest contribution to local emissions occurred in the summer, with emissions reaching $1.7–2.1 \times 10^{16}$ molecules cm^{-2}. Regional transport contributed 26% toward NO_2 concentrations during winter under the influence of the northeast wind and the transport channel along the Changbai Mountains in NEC. The contribution of industrial sources toward the NO_2 concentrations was higher than the contribution of vehicle exhaust in all the seasons due to massive fossil fuel combustion by intensive industrial activity. The contribution of industrial sources toward the NO_2 concentrations was significantly higher in winter than in other seasons due to the increased coal combustion for heating. Thus, it is important to reduce local emissions and strengthen regional collaborative governance to improve the air quality in Shenyang.

Author statement

Feng Liu: Conceptualization, Methodology, Investigation, Formal analysis, Writing – original draft, **Chengzhi Xing:** Conceptualization, Methodology, Writing – original draft, Writing – review & editing, **Pinjie Su:** Investigation, Writing – review & editing, **Yifu Luo:** Methodology, Investigation, **Ting Zhao:** Investigation, Formal analysis, **Jiexiao Xue:** Investigation, Formal analysis, **Guohui Zhang:**

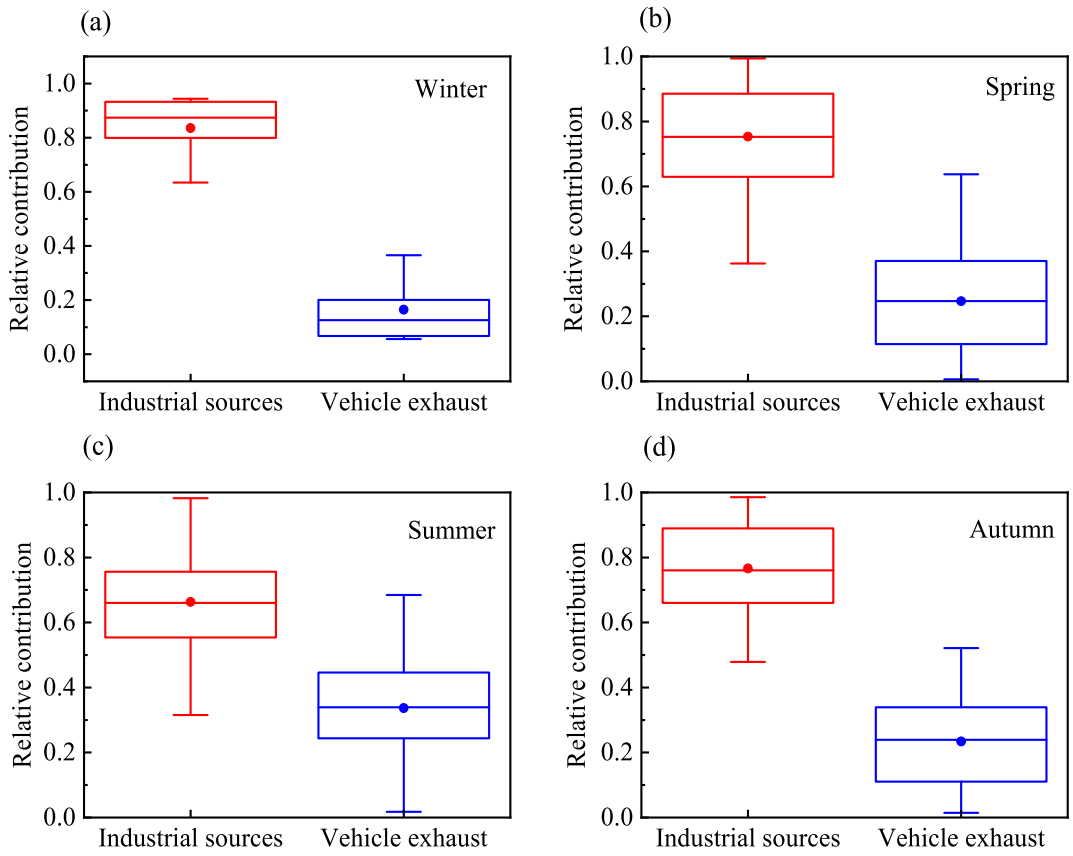

Fig. 8. Relative contributions of industrial sources and vehicle exhaust toward ambient NO_2 concentrations over Shenyang. The bottom and top of the box represent the 25th and 75th percentiles, respectively; the lines inside the boxes represent the medians; the dots represent the mean values; and the whiskers below and above the box denote the 10th and 90th percentiles, respectively.

Conceptualization, Investigation, **Sida Qin:** Methodology, Formal analysis, **Youtao Song:** Methodology, Investigation, **Naishun Bu:** Conceptualization, Investigation, Supervision, Writing – review & editing, Funding acquisition

Declaration of competing interest

The authors declare that they have no known competing financial interests or personal relationships that could have appeared to influence the work reported in this paper.

Acknowledgments

This work was supported by the National Key Research and Development Project of China [grant number 2018YFC1801200], the National Science Foundation of China [grant number 31972522], the Major Science and Technology Project of Liaoning Province [grant number 2019JH1/10300001], the Scientific Research Fund of the Liaoning Provincial Education Department [grant number LQN202003], the Liaoning Revitalization Talents Program [grant number XLYC2007032], the Open Research Fund of Key Laboratory of Wetland Ecology and Environment Research in Cold Regions of Heilongjiang Province [grant number 201903], the Presidential Foundation of the Hefei Institutes of Physical Science, Chinese Academy of Sciences, China [grant number YZJJ2021QN06], the Research Fund Program of the Guangdong-Hongkong-Macau Joint Laboratory of Collaborative Innovation for Environmental Quality [grant number GHML2021-102], and the National Key Research and Development Program of China [grant number 2017YFC0212500]. We thank the Belgian Institute for Space Aeronomy (BIRA-IASB), Brussels, Belgium, for their freely accessible QDOAS software (http://uv-vis.aeronomie.be/software/QDOAS/). We also appreciate the use of OMI NO_2 data from the NASA Goddard Earth Sciences Data and Information Services Center (GES-DISC) (https://disc.gsfc.nasa.gov/). We appreciate the CNEMC network stations for providing PM concentrations data (http://www.cnemc.cn/). We thank LetPub (www.letpub.com) for its linguistic assistance during the preparation of this manuscript.

Appendix A. Supplementary data

Supplementary data to this article can be found online at https://doi.org/10.1016/j.envpol.2022.119424.

References

Adame, J.A., Gutierrez-Alvarez, I., Bolivar, J.P., Yela, M., 2020. Ground-based and OMI-TROPOMI NO_2 measurements at El Arenosillo observatory: unexpected upward trends. Environ. Pollut. 264, 114771. https://doi.org/10.1016/j.envpol.2020.114771.

Aliwell, S.R., Roozendael, M.V., Johnston, P.V., Richter, A., Wagner, T., Arlander, D.W., Burrows, J.P., Fish, D.J., Jones, R.L., Tørnkvist, K.K., Lambert, J.-C., Pfeilsticker, K., Pundt, I., 2002. Analysis for BrO in zenith-sky spectra: an intercomparison exercise for analysis improvement. J. Geophys. Res. 107 https://doi.org/10.1029/2001jd000329. ACH-10.

Beirle, S., Platt, U., Wenig, M., Wagner, T., 2003. Weekly cycle of NO_2 by GOME measurements: a signature of anthropogenic sources. Atmos. Chem. Phys. 3, 2225–2232. https://doi.org/10.5194/acp-3-2225-2003.

Bogumil, K., Orphal, J., Homann, T., Voigt, S., Spietz, P., Fleischmann, O.C., Vogel, A., Hart-mann, M., Kromminga, H., Bovensmann, H., Frerick, J., Burrows, J.P., 2003. Measurements of molecular absorption spectra with the SCIAMACHY preflight model: instrument characterization and reference data for atmospheric remote-sensing in the 230–2380 nm region. J. Photochem. Photobiol., A 157, 167–184.

Chan, K., Wiegner, M., Geffen, J., Smedt, I.D., Alberti, C., Cheng, Z., Ye, S., Wenig, M., 2020. MAX-DOAS measurements of tropospheric NO_2 and HCHO in Munich and the comparison to OMI and TROPOMI satellite observations. Atmos. Meas. Tech. 13, 4499–4520. https://doi.org/10.5194/amt-13-4499-2020.

Chan, K.L., Wiegner, M., Wenig, M., Pöhler, D., 2018. Observations of tropospheric aerosols and NO_2 in Hong Kong over 5 years using ground based MAX-DOAS. Sci. Total Environ. 619–620, 1545–1556. https://doi.org/10.1016/j.scitotenv.2017.10.153.

Cheng, S., Ma, J., Cheng, W., Yan, P., Zhou, H., Zhou, L., Yang, P., 2019. Tropospheric NO_2 vertical column densities retrieved from ground-based MAX-DOAS measurements at Shangdianzi regional atmospheric background station in China. J. Environ. Sci. 80, 186–196. https://doi.org/10.1016/j.jes.2018.12.012.

Crutzen, P.J., 1970. The influence of nitrogen oxides on the atmospheric ozone content. Q. J. Roy. Meteorol. Soc. 96, 320–325.

Feng, R., Wang, Q., Huang, C., Liang, J., Luo, K., Fan, J., Cen, K., 2019. Investigation on air pollution control strategy in Hangzhou for post-G20/pre-Asian-games period (2018–2020). Atmos. Pollut. Res. 10, 197–208. https://doi.org/10.1016/j.apr.2018.07.006.

Fleischmann, O.C., Hartmann, M., Burrows, J. P., Orphal, J., 2004. New ultraviolet absorption cross-sections of BrO at atmospheric temperatures measured by time-windowing Fourier transform spectroscopy. Journal of Photochemistry and Photobiology A: Chemistry 168 (1–2), 117–132. https://doi.org/10.1016/j.jphotochem.2004.03.026.

Gao, C., Xiu, A., Zhang, X., Chen, W., Liu, Y., Zhao, H., Zhang, S., 2020. Spatiotemporal characteristics of ozone pollution and policy implications in Northeast China. Atmos. Pollut. Res. 11, 357–369. https://doi.org/10.1016/j.apr.2019.11.008.

Guo, J., He, J., Liu, H., Miao, Y., Liu, H., Zhai, P., 2016. Impact of various emission control schemes on air quality using WRF-Chem during APEC China 2014. Atmos. Environ. 140, 311–319. https://doi.org/10.1016/j.atmosenv.2016.05.046.

Hendrick, F., Müller, J.F., Clémer, K., Wang, P., De Mazière, M., Fayt, C., Gielen, C., Hermans, C., Ma, J.Z., Pinardi, G., Stavrakou, T., Vlemmix, T., Van Roozendael, M., 2014. Four years of ground-based MAX-DOAS observations of HONO and NO_2 in the Beijing area. Atmos. Chem. Phys. 14, 765–781. https://doi.org/10.5194/acp-14-765-2014.

Hönninger, G., Friedeburg, C.v., Platt, U., 2004. Multi axis differential optical absorption spectroscopy (MAX-DOAS). Atmos. Chem. Phys. 4, 231–254.

Hong, Q., Liu, C., Chan, K.L., Hu, Q., Xie, Z., Liu, H., Si, F., Liu, J., 2018. Ship-based MAX-DOAS measurements of tropospheric NO_2, SO_2, and HCHO distribution along the Yangtze River. Atmos. Chem. Phys. 18, 5931–5951. https://doi.org/10.5194/acp-18-5931-2018.

Hong, Q., Liu, C., Hu, Q., Xing, C., Tan, W., Liu, H., Huang, Y., Zhu, Y., Zhang, J., Geng, T., Liu, J., 2019. Evolution of the vertical structure of air pollutants during winter heavy pollution episodes: the role of regional transport and potential sources. Atmos. Res. 228, 206–222. https://doi.org/10.1016/j.atmosres.2019.05.016.

Javed, Z., Liu, C., Ullah, K., Tan, W., Xing, C. Z. and Liu, H. R., 2019. Investigating the Effect of Different Meteorological Conditions on MAX-DOAS Observations of NO_2 and CHOCHO in Hefei, China. Atmosphere. 10, 353. https://doi.org/10.3390/atmos10070353.

Jeong, U., Kim, J., Lee, H., Lee, Y.G., 2017. Assessing the effect of long-range pollutant transportation on air quality in Seoul using the conditional potential source contribution function method. Atmos. Environ. 150, 33–44. https://doi.org/10.1016/j.atmosenv.2016.11.017.

Lamsal, L.N., Krotkov, N.A., Celarier, E.A., Swartz, W.H., Pickering, K.E., Bucsela, E.J., Gleason, J.F., Martin, R.V., Philip, S., Irie, H., Cede, A., Herman, J., Weinheimer, A., Szykman, J.J., Knepp, T.N., 2014. Evaluation of OMI operational standard NO2 column retrievals using in situ and surface-based NO2 observations. Atmos. Chem. Phys. 14, 11587–11609. https://doi.org/10.5194/acp-14-11587-2014.

Lelieveld, J., Peters, W., Dentener, F.J., Krol, M.C., 2002. Stability of tropospheric hydroxyl chemistry. J. Geophys. Res. Atmos. 107. ACH-17-11.

Letu, H., Nakajima, T.Y., Wang, T., Shang, H., Ma, R., Yang, K., Baran, A.J., Riedi, J., Ishimoto, H., Yoshida, M., Shi, C., Khatri, P., Du, Y.H., Chen, L.F., Shi, J., 2021. A new benchmark for surface radiation products over the East Asia-Pacific region retrieved from the Himawari-8/AHI next-generation geostationary satellite. Bull. Am. Meteorol. Soc. 1–40. https://doi.org/10.1175/BAMS-D-20-0148.1.

Li, B., Shi, X.F., Liu, Y.P., Lu, L., Wang, G.L., Thapa, S., Sun, X.Z., Fu, D.L., Wang, K., Qi, H., 2020a. Long-term characteristics of criteria air pollutants in megacities of Harbin-Changchun megalopolis, Northeast China: spatiotemporal variations, source analysis, and meteorological effects. Environ. Pollut. 267, 115441. https://doi.org/10.1016/j.envpol.2020.115441.

Li, C., Liu, M., Hu, Y., Zhou, R., Huang, N., Wu, W., Liu, C., 2020b. Spatial distribution characteristics of gaseous pollutants and particulate matter inside a city in the heating season of Northeast China. Sustain. Cities Soc. 61, 102302. https://doi.org/10.1016/j.scs.2020.102302.

Li, X., Brauers, T., Hofzumahaus, A., Lu, K., Li, Y., Shao, M., Wagner, T., Wahner, A., 2012. MAX-DOAS measurements of NO_2, HCHO and CHOCHO at a rural site in Southern China. Atmos. Chem. Phys. 13, 2133–2151. https://doi.org/10.5194/acp-13-2133-2013.

Li, Y., Ye, C., Liu, J., Zhu, Y., Wang, J., Tan, Z., Lin, W., Zeng, L., Zhu, T., 2016. Observation of regional air pollutant transport between the megacity Beijing and the North China Plain. Atmos. Chem. Phys. 16, 14265–14283. https://doi.org/10.5194/acp-16-14265-2016.

Li, Z., Walters, W.W., Hastings, M.G., Song, L., Liu, D., Zhang, W., Pan, Y., Fu, P., Zhang, Y., Fang, Y., 2019. Nitrate isotopic composition in precipitation at a Chinese megacity: seasonal variations, atmospheric processes, and implications for sources. Earth Space Sci. 6, 2200–2213. https://doi.org/10.1029/2019EA000759.

Ma, Y.F., Du, B.Y., Wang, Q., Hu, Q.Q., Bian, Y.S., Wang, M.B., Jin, S.Y., 2019. Analysis of the atmospheric pollution transport pathways and sources in Shenyang, based on the HYSPLIT model. IOP Conf. Ser. Earth Environ. Sci. 351, 012030 https://doi.org/10.1088/1755-1315/351/1/012030.

Miao, Y., Guo, J., Liu, S., Zhao, C., Li, X., Zhang, G., Wei, W., Ma, Y., 2018. Impacts of synoptic condition and planetary boundary layer structure on the trans-boundary aerosol transport from Beijing-Tianjin-Hebei region to northeast China. Atmos. Environ. 181, 1–11. https://doi.org/10.1016/j.atmosenv.2018.03.005.

Ou, J., Hu, Q., Liu, H., Hong, Q., Xing, C., Tan, W., Lin, H., Wang, X., Xu, H., Zhu, P., Liu, W., 2021. Vertical characterization and potential sources of aerosols in different seasons over the Yangtze River Delta using ground-based MAX-DOAS. Environ. Pollut. 279, 116898. https://doi.org/10.1016/j.envpol.2021.116898.

Platt, U., Stutz, J., 2008. Differential Optical Absorption Spectroscopy - Principles and Applications. Springer, Berlin.

Quan, J., Dou, Y., Zhao, X., Liu, Q., Sun, Z., Pan, Y., Jia, X., Cheng, Z., Ma, P., Su, J., Xin, J., Liu, Y., 2020. Regional atmospheric pollutant transport mechanisms over the North China Plain driven by topography and planetary boundary layer processes. Atmos. Environ. 221, 117098. https://doi.org/10.1016/j.atmosenv.2019.117098.

Rollins, A.W., Browne, E.C., Min, K.E., Pusede, S.E., Wooldridge, P.J., Gentner, D.R., Goldstein, A.H., Liu, S., Day, D.A., Russell, L.M., Cohen, R.C., 2012. Evidence for NOx control over night time SOA formation. Science 337, 1210–1212. https://doi.org/10.1126/science.1221520.

Serdyuchenko, A., Gorshelev, V., Weber, M., Chehade, W., Burrows, J.P., 2014. High spectral resolution ozone absorption cross-sections-Part 2: temperature dependence. Atmos. Meas. Tech. 7, 625–636. https://doi.org/10.5194/amt-7-625-2014.

Shen, Y., Jiang, F., Feng, S., Zheng, Y., Cai, Z., Lyu, X., 2021. Impact of weather and emission changes on NO_2 concentrations in China during 2014-2019. Environ. Pollut. 269, 116163. https://doi.org/10.1016/j.envpol.2020.116163.

Song, H., Zhang, Y., Luo, M., Gu, J., Wu, M., Xu, D., Xu, G., Ma, L., 2019. Seasonal variation, sources and health risk assessment of polycyclic aromatic hydrocarbons in different particle fractions of $PM_{2.5}$ in Beijing, China. Atmos. Pollut. Res. 10, 105–114. https://doi.org/10.1016/j.apr.2018.06.012.

Song, Y.Z., Yang, H.L., Peng, J.H., Song, Y.R., Sun, Q., Li, Y., 2015. Estimating $PM_{2.5}$ concentrations in Xi'an city using a generalized additive model with multi-source monitoring data. PLoS One 10, e0142149. https://doi.org/10.1371/journal.pone.0142149.

Statistical Yearbook of Shenyang, 2020. http://tjj.shenyang.gov.cn/html/SYTJJ/15620336218981/15620336218981/15620336218981/3621898100319937.html, last access: 18 April 2021.

Stavrakou, T., Müller, J.F., Boersma, K.F., van der, A.R.J., Kurokawa, J., Ohara, T., et al., 2013. Key chemical NO_x sink uncertainties and how they influence top-down emissions of nitrogen oxides. Atmos. Chem. Phys. 13, 9057–9082.

Takashima, H., Kanaya, Y., Irie, H., 2015. Spatiotemporal inhomogeneity in NO_2 over Fukuoka observed by ground-based MAX-DOAS. Atmos. Environ. 100, 117–123. https://doi.org/10.1016/j.atmosenv.2014.10.057.

Tan, W, Liu, C., Wang, S., Liu, H., Zhu, Y., Su, W., Hu, Q., Liu, J., 2020. Long-distance mobile MAX-DOAS observations of NO_2 and SO_2 over the North China Plain and identification of regional transport and power plant emissions. Atmos Res. 245, 105037. https://doi.org/10.1016/j.atmosres.2020.105037.

Tao, M., Chen, L., Su, L., Tao, J., 2012. Satellite observation of regional haze pollution over the North China Plain. J. Geophys. Res. Atmos. 117, D12203. https://doi.org/10.1029/2012jd017915.

Thalman, R., Volkamer, R., 2013. Temperature dependent absorption cross-sections of O_2-O_2 collision pairs between 340 and 630 nm and at atmospherically relevant pressure. Phys. Chem. Chem. Phys. 15, 15371–15381. https://doi.org/10.1039/c3cp50968k.

Tian, J., Fang, C., Qiu, J., Wang, J., 2020. Analysis of pollution characteristics and influencing factors of main pollutants in the atmosphere of Shenyang city. Atmosphere 11, 766–786. https://doi.org/10.3390/atmos11070766.

Valin, L.C., Russell, A.R., Cohen, R.C., 2013. Variations of OH radical in an urban plume inferred from NO_2 column measurements. Geophys. Res. Lett. 40, 1856–1860. https://doi.org/10.1002/grl.50267.

Vandaele, A.C., Hermans, C., Simon, P.C., Carleer, M., Colin, R., Fally, S., Merienne, M.F., Jenouvrier, A., Coquart, B., 1998. Measurements of the NO_2 absorption cross-section from 42,000 cm^{-1} to 10,000 cm^{-1} (238–1000 nm) at 220 K and 294 K. J. Quanr. Specrrosc. Radio. Trans. 59, 171–184. https://doi.org/10.1016/S0022-4073(97)00168-4.

Vlemmix, T., Piters, A.J.M., Berkhout, A.J.C., Gast, L.F.L., Wang, P., Levelt, P.F., 2011. Ability of the MAX-DOAS method to derive profile information for NO_2: can the boundary layer and free troposphere be separated? Atmos. Meas. Tech. 4, 2659–2684. https://doi.org/10.5194/amt-4-2659-2011.

Wang, C., Wang, T., Wang, P., Rakitin, V., 2020. Comparison and validation of TROPOMI and OMI NO_2 observations over China. Atmosphere 11, 636. https://doi.org/10.3390/atmos11060636.

Wang, Y., Lampel, J., Xie, P., Beirle, S., Li, A., Wu, D., Wagner, T., 2017. Ground-based MAX-DOAS observations of tropospheric aerosols, NO_2, SO_2 and HCHO in Wuxi, China, from 2011 to 2014. Atmos. Chem. Phys. 17, 2189–2215. https://doi.org/10.5194/acp-17-2189-2017.

Wittrock, F., Oetjen, H., Richter, A., Fietkau, S., Medeke, T., Rozanov, A., et al., 2004. MAX-DOAS measurements of atmospheric trace gases in Ny-Alesund – radiative transfer studies and their application. Atmos. Chem. Phys. 4, 955–966.

Wu, F., Xie, P., Li, A., Mou, F., Chen, H., Zhu, Y., Zhu, T., Liu, J., Liu, W., 2018. Investigations of temporal and spatial distribution of precursors SO_2 and NO_2 vertical columns in the North China Plain using mobile DOAS. Atmos. Chem. Phys. 18, 1535–1554. https://doi.org/10.5194/acp-18-1535-2018.

Wyche, K.P., Nichols, M., Parfitt, H., Beckett, P., Gregg, D.J., Smallbone, K.L., Monks, P. S., 2021. Changes in ambient air quality and atmospheric composition and reactivity in the South East of the UK as a result of the COVID-19 lockdown. Sci. Total Environ. 755, 142526. https://doi.org/10.1016/j.scitotenv.2020.142526.

Xing, C., Liu, C., Hu, Q., Fu, Q., Lin, H., Wang, S., Su, W., Wang, W., Javed, Z., Liu, J., 2020. Identifying the wintertime sources of volatile organic compounds (VOCs) from MAX-DOAS measured formaldehyde and glyoxal in Chongqing, southwest China. Sci. Total Environ. 715, 136258. https://doi.org/10.1016/j.scitotenv.2019.136258.

Xing, C., Liu, C., Wang, S., Chan, K.L., Gao, Y., Huang, X., Su, W., Zhang, C., Dong, Y., Fan, G., Zhang, T., Chen, Z., Hu, Q., Su, H., Xie, Z., Liu, J., 2017. Observations of the vertical distributions of summertime atmospheric pollutants and the corresponding ozone production in Shanghai, China. Atmos. Chem. Phys. 17, 14275–14289. https://doi.org/10.5194/acp-17-14275-2017.

Xing, C., Liu, C., Wang, S., Hu, Q., Liu, H., Tan, W., Zhang, W., Li, B., Liu, J., 2019. A new method to determine the aerosol optical properties from multiple-wavelength O_4 absorptions by MAX-DOAS observation. Atmos. Meas. Tech. 12, 3289–3302. https://doi.org/10.5194/amt-12-3289-2019.

Yang, H., Peng, Q., Zhou, J., Song, G., Gong, X., 2020. The unidirectional causality influence of factors on $PM_{2.5}$ in Shenyang city of China. Sci. Rep. 10, 1–12. https://doi.org/10.1038/s41598-020-65391-5.

Yang, T., Si, F., Luo, Y., Zhan, K., Wang, P., Zhou, H., Zhao, M., Liu, W., 2019. Source contribution analysis of tropospheric NO_2 based on two-dimensional MAX-DOAS measurements. Atmos. Environ. 210, 186–197. https://doi.org/10.1016/j.atmosenv.2019.04.058.

Zhang, C., Liu, C., Hu, Q., Cai, Z., Su, W., Xia, C., Zhu, Y., Wang, S., Liu, J., 2019. Satellite UV-Vis spectroscopy: implications for air quality trends and their driving forces in China during 2005–2017. Light Sci. Appl. 8, 2–12. https://doi.org/10.1038/s41377-019-0210-6.

Zhang, C., Liu, C., Chan, K. L., Hu, Q., Liu, H., Li, B., Xing, C., Tan, W., Zhou, H., Si, F. and Liu, J., 2020. First observation of tropospheric nitrogen dioxide from the Environmental Trace Gases Monitoring Instrument onboard the GaoFen-5 satellite. Light Sci Appl. 9, 1–9. https://doi.org/10.1038/s41377-020-0306-z.

Zhang, L., Lee, C.S., Zhang, R., Chen, L., 2017. Spatial and temporal evaluation of long term trend (2005–2014) of OMI retrieved NO_2 and SO_2 concentrations in Henan Province, China. Atmos. Environ. 154, 151–166. https://doi.org/10.1016/j.atmosenv.2016.11.067.

Zhao, H., Che, H., Zhang, L., Gui, K., Ma, Y., Wang, Y., Wang, H., Zheng, Y., Zhang, X., 2020. How aerosol transport from the North China plain contributes to air quality in northeast China. Sci. Total Environ. 738, 139555. https://doi.org/10.1016/j.scitotenv.2020.139555.